JOURNAL OF PROPULSION AND POWER
Vol. 21, No. 2, March–April 2005

Simulation Strategy of Turbulent Internal Flow in Solid Rocket Motor

B. Wasistho* and R. D. Moser†
University of Illinois at Urbana–Champaign, Urbana, Illinois 61801

A strategy for the simulation of turbulent internal flows in a solid rocket motor (SRM) is described. Sources of turbulence inside an SRM are identified and their dominance relative to each other is characterized to set a priority in the modeling effort. This complex problem is simplified by subdividing it into problem components allowing for a more detailed study of each component. Problems of interest in which investigations have been pursued are compressible periodic rockets, spatial transition in a laboratory-scale rocket, and effect of inhibitors and large-eddy simulation (LES) wall-layer modeling (WLM) for the nozzle boundary layer. Grid sensitivity is observed in the application of dynamic LES to a transitional flow in an SRM. Inhibitors at the segment juctions act as a trip in the transition to turbulence and play a more dominant role compared to the injection of turbulence from the propellant surface. Detached-eddy simulation provides relatively accurate wall gradient properties and is more generally applicable than WLM. This hybrid method, however, requires some degree of implicitness in the time discretization to be efficient.

Nomenclature

C_d	=	dynamic coefficient in large-eddy simulation (LES)
C_f	=	skin friction coefficient
C_p	=	specific heat at constant pressure, N · m/(kg · K)
e	=	total energy density, J/m^3
F_i	=	subgrid term in ith momentum equation
F_e	=	subgrid term in energy equation
L_{ij}	=	subgrid stress tensor in test filter level
M	=	Mach number
M_{ij}	=	modeled stress tensor in test filter level
Pr	=	Prandtl number
p	=	pressure, Pa
$\dot{q}$	=	heat transfer rate, kg/s^3
q_j	=	jth component of heat flux vector, kg/s^3
Re_b	=	Reynolds number based on bulk velocity
Re_{inj}	=	Reynolds number based on injection velocity
Re_τ	=	Reynolds number based on friction velocity
S	=	source term
S_{ij}	=	strain rate tensor, 1/s
S_t	=	strain rate
T	=	temperature, K
$\boldsymbol{u}$	=	velocity vector, m/s
u, v	=	streamwise and normal velocity, m/s
u_i	=	ith component of velocity vector $\boldsymbol{u}$, m/s
$\boldsymbol{v}$	=	Favre filtered velocity vector, m/s
$\boldsymbol{v}_i$	=	ith component of $\boldsymbol{v}$, m/s
x_j	=	jth component of Cartesian coordinate, m
Y	=	reference wall distance in wall layer model
α_i	=	ith energy subgrid term
β	=	constant in Sutherland formula
γ	=	adiabatic gas constant
ϵ	=	m_{inj}/m_b, injection to bulk mass rate ratio
ζ	=	spanwise component of body-fitted coordinate, m
η	=	wall-normal component of body-fitted coordinate, m
κ	=	filter width ratio due to test-basic consecutive filtering, von Karman constant
μ	=	dynamic viscosity, kg/(m · s)
ξ	=	streamwise component of body-fitted coordinate, m
ρ	=	density, kg/m^3
σ_{ij}	=	stress tensor, kg/(m · s^2)
χ	=	viscosity ratio in SA model

Subscripts

b	=	basic, in Spalart–Allmaras (SA) model
e	=	boundary layer edge, energy equation
eff	=	effective
inj	=	injection
mi	=	ith-component of momentum equation
r	=	density equation
s	=	streamwise direction
t	=	turbulent
w	=	wall

Superscripts

$+$	=	in wall units
-	=	basic filtered
~	=	Favre filtered
^	=	test filtered

I. Introduction

THE internal chamber of a segmented solid rocket booster constitutes a much more complex system than its external pencil-like shape, illustrated in Fig. 1, may suggest. As shown in Fig. 2, the chamber is divided into three segments by two inhibitors. A propellant block is attached to the case in each segment. A cavity is formed in each segment between the partly burned propellant and the inhibitor of the downstream segment. The chamber is bounded by a head-end wall at the front and a nozzle at the aft.

From this illustration, modeling the turbulence inside a solid rocket motor (SRM) is a challenging task because it should be able to tackle a broad range of flow phenomena that are impossible to handle using the single unified method currently available. During ignition, the jet flow coming from the igniter is transitioning into a turbulent state, convecting and diffusing the heat to the propellant surface, which in turn triggers the burning of the propellant. During the propellant burning, the flow in the chamber is driven by mass

Presented as Paper 2004-0263 at the AIAA Aerospace Sciences Meeting, Reno, NV, 5–8 January 2004; received 20 January 2004; revision received 10 June 2004; accepted for publication 1 June 2004.

*Research Scientist, Center for Simulation of Advanced Rockets; wasistho@uiuc.edu. Member AIAA.

†Professor, Department of Theoretical and Applied Mechanics, Center for Simulation of Advanced Rockets. Senior Member AIAA.

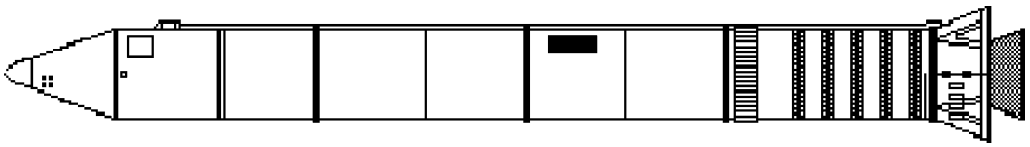

Fig. 1 Diagram of external image of segmented SRM.

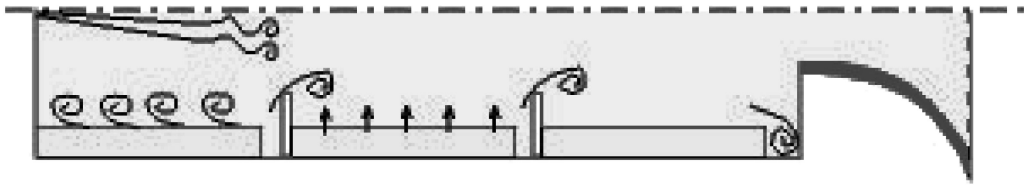

Fig. 2 Diagram of inside SRM chamber illustrating various sources of turbulence.

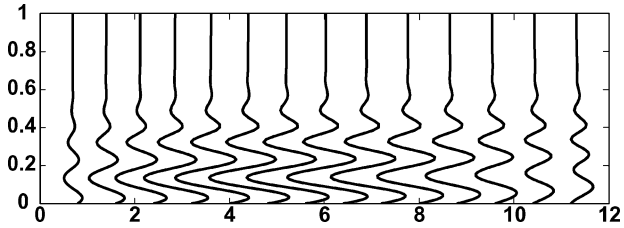

Fig. 3 Snapshot of unsteady axial velocity fluctuations in wall-normal direction in C0 geometry.

injection from the propellant surface. It is known that injection-driven flow has an inherent hydrodynamic instability in the laminar region and is convectively unstable.[1] The unstable layer near the injection wall forms backward-inclined vortices, as illustrated in Fig. 2 near the head end. The axial acoustic waves which present as pressure oscillations in the longitudinal direction generate a viscous acoustic layer near the wall in the laminar region. This acoustic layer, which is basically an unsteady axial velocity fluctuation in the wall-normal direction, is shown in Fig. 3. In this illustration, the pressure oscillation is forced at the outlet boundary. This acoustic layer forms another source of laminar instability. Furthermore, the mass injection from the burning propellant surface is nonuniform, which necessitates a refined injection modeling approach to physically transfer the small-scale fluctuations in the combustion layer to significantly larger scale fluid fluctuations.

Stagnation and separation phenomena also play dominant roles in the vicinity of the inhibitors. The flow separates from the inhibitor wall and there is vortex shedding. The cavity between the propellant and the inhibitor also induces flow circulations. The turbulent flow containing large-scale vortices from the vortex shedding impinges the nozzle wall, forming a stagnation, and then accelerates toward the outlet due to the nozzle expansion. The flow Mach number can evolve from 0.5 at the nozzle inlet up to nearly 3.0 at the outlet. This in turn generates a very thin highly compressible turbulent shear layer at the nozzle wall (dark layer in Fig. 2), presenting a challenge to accurately model the momentum and heat transfer. Besides the strong negative pressure gradient, the effect of surface roughness due to nozzle errosion has to be taken into account. These complex processes are very challenging for theoretical as well as numerical predictors.

Efforts in developing theoretical models of SRM internal flows have been made since at least half a century ago and have produced important advancements, especially in the past two decades. The profile of laminar flows bounded by porous walls was developed by Taylor[2] and constitutes a valid representation of the SRM internal flow in the head-end region. The effect of compressibility is incorporated in the theoretical relations of Balakrishnan et al.[3] Models for the viscous acoustic layer desribed in the preceding paragraph were derived by Flandro[4,5] and were further refined by other researchers.[6]

Advances in numerical simulations in recent years have enabled a more realistic represention of the effect of turbulence which was previously too difficult for theoretical modeling. Comparison of the aforementioned theoretical models and the corresponding numerical predictions has been performed by Wasistho et al.[7] Turbulence predictions in injection-driven flows using the Reynolds-averaged Navier–Stokes (RANS) approach were reported by Beddini,[8] Sabnis et al.,[9] and Chaouat and Schiestel,[10] among others. They suggest that only advanced models should be used for this type of flow. With regard to this, simulations based on a fully unsteady approach have been explored. Liou et al.[11] and Apte and Yang[12,13] conducted LES of the nozzleless laboratory-scale rocket experiment by Traineau et al.[14] Liou et al.[11] applied the basic Smagorinsky subgrid scale (SGS) model with a near-wall damping to the transitional flow case in two dimensions. It is known, however, that nondynamic SGS models such as the basic Smagorinsky model cannot handle transition adequately. Moreover, the two-dimensional environment hinders adequate representation of the turbulence structures. LES is an inherently three-dimensional method, unlike RANS where the homogeneous direction is statistically modeled. Moreover, three-dimensional simulation[7] shows that the x, y, and z vorticity components are of comparable magnitude in the turbulent region of an SRM, although the spanwise component is the strongest. In two dimensions, the x and y components would vanish. A similar SGS model has been used in a three-dimensional simulation by Apte and Yang.[12] A dynamic LES approach is used in their recent work[13] with a very high grid resolution (9 million points). We use the same approach in our study, however with an order-of-magnitude smaller grid resolution (fewer than 1 million points). This poses a greater challenge to the SGS model. The simplest model problem for rocket flow is injection-driven flow with periodicity in the wall parallel directions, in effect a channel flow with mass injection from the walls. Nicoud et al.[15] performed detailed turbulence analysis of a periodic wall-injection flow. The problem setup in his study, however, requires the use of a specific freestream boundary condition opposite to the wall, through which the mass injected from the wall is removed from the domain to retain the mass conservation. This is inconsistent with the real flow condition in an SRM, where the mass flow through a downstream axial plane is always larger than that through an upstream plane. Moreover, in a planar rocket, for instance, the averaged mass flow through the centerplane parallel to the wall is zero. To avoid this inconsistency, we employ in our similar model problem, called a compressible periodic rocket (CPR), a full computational domain with the upper and lower boundary being the injection walls and we impose a source term in the continuity equation for the mass conservation.[1]

The objective of this study is first to propose a strategy for tackling the various modeling challenges described in the beginning of this section and, second, to compare our findings with those reported by others on a similar subject and assess the sensitivity of the results to the different approaches. It should be noted that this study

serves as an overview of research activities in the Center for Simulation of Advanced Rockets (CSAR) in dealing with turbulence in an SRM; therefore, methods and results are presented in brief. In-depth analysis for each problem case will be reported separately.

The paper is organized as follows. In Sec. II we outline a strategy in simulating turbulence in an SRM. The governing fluid equations, various turbulence models, and additional terms due to specific flow cases are described in Sec. III. Section IV is divided into subsections discussing results of each validation case. We summarize our findings and recommendations in Sec. V.

II. Simulation Strategy

To tackle the various modeling challenges described in the preceding section, a zonal modeling approach is followed. In general, a dynamic LES is employed in the rocket core flow, motivated by the fact that the turbulence structures are more or less homogeneous in the region away from the wall. Moreover, the dynamic LES has the capability of capturing transition in a natural way. Near the walls, we attach a wall layer model to the LES or apply detached eddy simulation (DES),[16] which models all turbulence scales near the wall and acts as a subgrid model farther from the wall, where the wall distance becomes larger than the local grid size. Note that the near-wall model is used only at the no-slip wall of the nozzle; no wall model is employed at the injection wall. DES is appropriate for use in the entire nozzle flow, because the underlying RANS approach can handle stagnation, heat transfer, surface roughness, and freestream turbulence intrinsically.

The complex problem of integrated SRM simulation is subdivided into simplified yet well-defined components of investigation. Appropriate simulation tools and specific test cases for each component are selected. This subdivision is outlined in Table 1. Corresponding to each test case is a simplified flow domain, schematically represented in Fig. 4. The six configurations are specific for Case 0 (C0), CPR, channel flow, Case ONERA-86 (O86), O86 with inhibitors (O86i), and Case 1 (C1) test cases, respectively. CPR is used for the linear stability validation by comparing no-model NS (two-dimension or three-dimensional) with the linear stability theory. It also serves as a test case for the validation of SGS models in temporal transition studies and for modeling the injection turbulence. C0 is used for the study of the acoustic properties of the flow. O86 forms a test case for LES validation in an injection induced spatial transition. O86i has a configuration similar to that of O86, except that inhibitors are mounted at the top and bottom walls in the laminar region. It is designed to investigate the effect of the inhibitors and their dominance in generating turbulence compared to the injection fluctuations. Channel flow and nozzle simulations serve as validation cases of various wall-layer models and DES in predicting the boundary-layer momentum and heat transfer in zero and finite pressure gradient, respectively. These test cases are also used in the validation of the interface layer between RANS or DES on one side and LES on the other side. In addition, the channel flow is used as a standard validation case for contemporary LES models such as the optimal LES.[17] Finally, the C1 case is suitable to test the model prediction of the dominant frequencies present in the flow, especially due to vortex shedding and acoustics. It also serves as a validation case for multiphase LES (MPLES), with and without propellant burning.

Table 1 Subdivision of turbulence modeling in SRM into problems of interest, testbeds and tools

Problem	Testbed	Tools	Reference
1. Hydrodynamic stability	CPR	No-model NS	Linear stability theory
2. Acoustic effects	C0	No-model NS	Acoustic model
3. SGS model test in temporal transition	CPR	LES	DNS
4. Application in spatial transition	O86	LES	Experiment
5. Modeling injection turbulence	CPR O86	LES	Parametric
6. Effect of inhibitors	O86i	LES	LES O86
7. Modeling nozzle boundary layer, heat transfer and RANS–LES interface layer	Channel nozzle	LES + wlm DES	DNS Experiment Parametric
8. Multiphase LES	Channel C1	MPLES	Experiment Other sim.
9. Optimal LES	Isotropic channel	Optimal LES	DNS

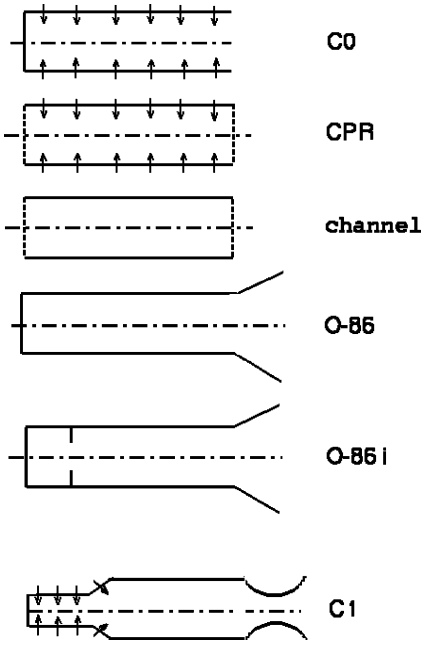

Fig. 4 Simplified model configurations for detailed study of various problems of interest.

III. Governing Equations

The internal rocket chamber flow is governed by the time-dependent compressible Navier–Stokes (NS) equations representing the conservation of mass, momentum, and energy:

$$\partial_t \rho + \partial_j(\rho u_j) = S_r \tag{1}$$

$$\partial_t(\rho u_i) + \partial_j(\rho u_i u_j) + \partial_i p - \partial_j \sigma_{ij} = S_{mi} \tag{2}$$

$$\partial_t e + \partial_j[(e+p)u_j] - \partial_j(\sigma_{ij}u_i - q_j) = S_e \tag{3}$$

The summation convention is used throughout this paper. The symbols ∂_t and ∂_j denote the partial differential operators $\partial/\partial t$ and $\partial/\partial x_j$, ρ is the density, p is the pressure, u_i is the ith component of the velocity vector, and e is the total energy density, given for an ideal gas by

$$e = p/(\gamma - 1) + \tfrac{1}{2}\rho u_i u_i \tag{4}$$

where γ denotes the adiabatic gas constant, set to 1.4. The stress tensor σ_{ij} is a function of the dynamic viscosity μ and the strain rate tensor:

$$\sigma_{ij} = \mu(T) S_{ij} \tag{5}$$

where the strain rate tensor S_{ij} is defined as

$$S_{ij} = \partial_j u_i + \partial_i u_j - \tfrac{2}{3}\delta_{ij}\partial_k u_k \tag{6}$$

The heat flux vector q_j is defined as

$$q_j = -(\mu C_p/Pr)\partial_j T \tag{7}$$

where C_p is the specific heat at constant pressure, while the molecular Prandtl number is set to 0.72. The contribution of turbulent Prandtl number appears through the subgrid energy modeling described in Sec. III. B. The relation among temperature, density, and pressure follows the ideal gas law. Sutherland's law is applied in computing the dynamic viscosity μ as a function of temperature:

$$\mu(T) = \beta/(T + C)T^{\frac{3}{2}} \tag{8}$$

where $C = 110.4$ K and $\beta = 1.456 \cdot 10^{-6}$ kg/ms.

The right-hand sides S_r, S_{mi}, and S_e are source terms of conservation equations (1–3), respectively, which are nonzero for the CPR case due to the homogenization procedure used to account for streamwise growth. These source terms, which represent the evolution rate of the mass, momentum, and energy, read as follows[1]:

$$S_r = -\epsilon\langle \rho u_1 \rangle \tag{9}$$

$$S_{mi} = -\epsilon\left\langle \rho u_1 u_i + \delta_{i1}\left(\rho u_1^2 + \partial_s p\right)\right\rangle \tag{10}$$

$$S_e = -\epsilon\langle (e + p)u_j \rangle \tag{11}$$

where angle brackets denote averaging over the homogeneous directions (stream- and spanwise) and $\epsilon = m_{\text{inj}}/m_b$ is the ratio between the injection and bulk mass rate. The quantity $\partial_s p = \partial p/\partial x_s$, where $x_s = \epsilon x$, is the pressure gradient to be determined from the mass flux balance. Physically, S_r compensates for the mass added through the injection walls, whereas S_{mi} and S_e balance the acceleration and the corresponding increase of energy due to the increase in mass flux in the streamwise direction.

For the channel flow, only S_{m1} is nonzero, consisting of just the streamwise pressure gradient as the mean flow driving force. We compute the pressure gradient from the mass flux balance using the bulk mass flux derived from Dean's correlations[18] as a reference instead of the conventional way of setting it equal to the average wall stress divided by the channel height. For test cases other than CPR and channel flow, the source terms are zero.

The equations are discretized explicitly in time using a four-step Runge–Kutta method. A second-order finite volume central scheme is used for the spatial discretization, following the method of Jameson et al.[19] to retain the conservative character of the discretized equations. The viscous terms are treated by defining auxiliary control volumes that are staggered to the primary control volumes in each direction. We use Rocflo,[20] a block-structured code developed at CSAR, as the base code in this study and add the viscous and turbulence capabilities to it. For complex physics and geometry typically found in rocket applications, further investigations are required to assess the efficiency of higher order treatments, considering the fact that the numerical accuracy of other components interacting with the fluid component, such as combustion and solid structure, is typically second order. Moreover, it has been shown that the second-order method produces reasonable results,[21,22] provided that the mesh resolution is sufficient, which can be assessed through a mesh refinement study. In the context of this further extension to a realistic rocket application, we use the second-order method in the present study. A higher order method will be used for the turbulence analysis of each test case in more detail.

In the LES approach, the NS equations are spatially filtered. We used the top-hat filter in our simulations.[23] The filtered NS equations, assuming zero source terms for convenience, read as follows:

$$\partial_t \bar{\rho} + \partial_j(\bar{\rho}\tilde{u}_j) = 0 \tag{12}$$

$$\partial_t(\bar{\rho}\tilde{u}_i) + \partial_j(\bar{\rho}\tilde{u}_i\tilde{u}_j) + \partial_i \bar{p} - \partial_j \breve{\sigma}_{ij} = F_i \tag{13}$$

$$\partial_t \breve{e} + \partial_j[(\breve{e} + \bar{p})\tilde{u}_j] - \partial_j(\breve{\sigma}_{ij}\tilde{u}_i - \breve{q}_j) = F_e \tag{14}$$

where the additional momentum and energy subgrid terms appearing on the right-hand side are given by

$$F_i = -\partial_j(\bar{\rho}\tau_{ij}) \tag{15}$$

$$F_e = \alpha_1 + \alpha_2 + \alpha_3 + \alpha_4 \tag{16}$$

with $\bar{\rho}\tau_{ij} = \bar{\rho}(\widetilde{u_i u_j} - \tilde{u}_i\tilde{u}_j)$. The basic filter operation is denoted by an overbar, whereas a tilde indicates Favre filtering.[24] Quantities denoted by $(\breve{\cdot})$ have the same original expressions but in filtered variables. The term $\partial_j(\bar{\sigma}_{ij} - \breve{\sigma}_{ij})$ is dropped from F_i because it is negligible compared to $\partial_j(\bar{\rho}\tau_{ij})$.[25] The energy subgrid term is composed of several components,[26] which are α_1, the kinetic energy transfer from resolved to subgrid scales; α_2, the effect of subgrid turbulence on the resolved heat conduction; α_3, the pressure dilatation; and α_4, the subgrid turbulence dissipation rate.

A. Subgrid Stress Models

The turbulent or subgrid stress tensor $\bar{\rho}\tau_{ij}$ is modeled by the dynamic eddy viscosity model:

$$\bar{\rho}\tau_{ij} = -\bar{\rho}C_d\Delta^2|S(\tilde{\mathbf{u}})|S_{ij}(\tilde{\mathbf{u}}) \tag{17}$$

The model coefficient, unlike in the basic Smagorinsky model, is dynamically determined by substituting the preceding expression into the Germano identity.[27] This results in

$$C_d M_{ij} = L_{ij} \tag{18}$$

with

$$M_{ij} = -\hat{\bar{\rho}}(\kappa\Delta)^2|S(\boldsymbol{v})|S_{ij}(\boldsymbol{v}) + \left[\bar{\rho}\Delta^2|S(\tilde{u})|S_{ij}(\tilde{u})\right]\hat{} \tag{19}$$

and

$$L_{ij} = (\overline{\rho u_i}\,\overline{\rho u_j}/\bar{\rho})\hat{} - \widehat{\overline{\rho u_i}}\,\widehat{\overline{\rho u_j}}/\hat{\bar{\rho}} \tag{20}$$

The filter operator $\widehat{(\cdot)}$ represents a test filtering of the basic filtered quantity. For convenience, the superscript $\hat{}$ is used to indicate that the test filter is applied to the expression inside the enclosures. The test filter width is twice the basic filter width. The ratio of the filter width associated with the consecutive application of the test and basic filtering to that of the basic filter is represented by κ in Eq. (19). For the top-hat filter used in our filtering, it can be shown that $\kappa = \sqrt{5}$ gives an optimal approximation.[23] The notation $\boldsymbol{v}$ in Eq. (19) is the Favre-filtered velocity at the test filter level and $|S(\boldsymbol{v})|$ is the strain rate magnitude based on this velocity,

$$v_i = \widehat{\overline{\rho u_i}}/\widehat{\bar{\rho}} \qquad \text{and} \qquad |S(\boldsymbol{v})|^2 = \tfrac{1}{2}S_{ij}^2(\boldsymbol{v}) \tag{21}$$

The expression for the strain rate tensor is given by Eq. (6). Using a least-squares approach,[28] the dynamic coefficient is approximated by

$$C_d = \max\left(0, \frac{\langle M_{ij}L_{ij}\rangle}{\langle M_{ij}M_{ij}\rangle}\right) \tag{22}$$

Note that the numerator and denominator in the preceding equation are averaged over the homogeneous directions or by employing a local filtering, which is expressed by the angle brackets to prevent numerical instability caused by negative values of C_a. In addition, the model coefficient in Eq. (22) is constrained to be nonnegative.

B. Subgrid Energy Models

In the modeling of the energy subgrid terms, the kinetic-energy transfer term α_1 can be computed directly from the model for the turbulent stress tensor $\bar{\rho}\tau_{ij}$ in the momentum equation. This term is expressed as

$$\alpha_1 = \tilde{u}_i\partial_j(\bar{\rho}\tau_{ij}) \tag{23}$$

The sum of the heat conduction and pressure dilatation terms is lumped together using the turbulent heat conductivity model,[29] similar to Eq. (7):

$$\alpha_2 + \alpha_3 = -(\mu_t C_p/Pr_t)\partial_j T \tag{24}$$

where μ_t is the modeled eddy viscosity and Pr_t the turbulent Prandtl number, set to 0.9 rather than determined dynamically. The dissipation rate term α_4 is modeled using the k equation model,[30]

$$\alpha_4 = c_\epsilon \bar{\rho}\left(k^{\frac{3}{2}}\Big/\Delta\right) \tag{25}$$

where $k = 1/2\tau_{ii}$ and c_ϵ is determined dynamically by assuming a global balance between the kinetic energy transfer and the dissipation rate.

C. Reynolds-Averaged Navier–Stokes Spalart-Allmaras Model

In addition to LES, we provide the option of using a RANS approach. Instead of filtering the NS equations, in RANS the equations are ensemble averaged. This results in the requirement to model the Reynolds stress term $\rho u_i' u_j'$ in the momentum equation, where u_i' is the ith component of fluctuating velocity about the averaged value. Following the eddy viscosity principle of relating Reynolds stress to the strain rate tensor S_{ij},

$$\rho u_i' u_j' = \mu_t S_{ij} \tag{26}$$

We employ the SA model for the eddy viscosity μ_t. The SA model is a one-equation model by Spalart and Allmaras[31] originally developed for the external aerodynamic flow environment. We follow the compressible version of this model in which a transport equation for $\rho\tilde{\nu}$ is solved, where ρ is the density and $\tilde{\nu}$ is a working variable:

$$\partial_t \rho\tilde{\nu} + \partial_j(u_j\rho\tilde{\nu}) = C_{b1}\rho\tilde{\nu}\tilde{\Omega} - c_{w1}f_w\rho(\tilde{\nu}/d)^2 + (\rho c_{b2}/\sigma)(\partial_j\tilde{\nu})^2 + (1/\sigma)\partial_j((\rho\tilde{\nu}+\mu)\partial_j\tilde{\nu}) \tag{27}$$

The eddy viscosity is related to $\tilde{\nu}$ by

$$\mu_t = \rho\tilde{\nu}f_{v1}, \qquad f_{v1} = \chi^3\Big/\left(\chi^3 + c_{v1}^3\right), \qquad \chi = \rho\tilde{\nu}/\mu \tag{28}$$

The production term $\tilde{\Omega}$ is given by

$$\tilde{\Omega} = \Omega + (\tilde{\nu}/\kappa^2 d^2)f_{v2}, \qquad f_{v2} = 1 - \chi/(1+\chi f_{v1}) \tag{29}$$

where Ω is the vorticity magnitude. The blending function f_w reads as follows:

$$f_w = g\left(\frac{1+c_{w3}^6}{g^6+c_{w3}^6}\right)^{\frac{1}{6}}, \qquad g = r + c_{w2}(r^6 - r) \tag{30}$$

$$r = \min\left(\frac{\tilde{\nu}}{\tilde{\Omega}\kappa^2 d^2}, 10\right) \tag{31}$$

The second term on the right-hand side represents the destruction term. The model coefficents are as follows:

$$c_{b1} = 0.1355, \qquad \sigma = \tfrac{2}{3}, \qquad c_{b2} = 0.622, \qquad \kappa = 0.41$$

$$c_{w1} = c_{b1}\Big/\kappa^2 + (1+c_{b2})/\sigma, \qquad c_{w2} = 0.3$$

$$c_{w3} = 2, \qquad c_{v1} = 7.1$$

D. Detatched Eddy Simulation

DES was derived originally from the SA model described earlier. It is designed to operate as an SGS model away from the wall; in effect it models the turbulence motions smaller than the local grid size and naturally switches to RANS near the wall, where it models all scales of turbulence. Similar to LES, DES can be viewed as a three-dimensional subgrid model but with the near-wall model intrinsicly built in. The advantage of DES over LES is that a typical RANS grid resolution near the wall is sufficient. Only the resolution in the wall-normal direction scales with wall units. In LES, this near-wall restriction applies in all coordinate directions. On the other hand, because DES is derived from RANS rather than from the filtered NS, it hinders the addition of other subgrid effects in a rigorous way. Such requirements appear when we consider multiphase flow.

The DES modification with respect to SA concerns the length scales d in the destruction term, represented in Eq. (27) by

$$\partial_t c_{w1} f_w \rho(\tilde{\nu}/d)^2 \tag{32}$$

In the RANS mode, d is the distance to the nearest wall, which represents the damping of turbulence by the wall. In DES, d is replaced by $\tilde{d}$, which is given by

$$\tilde{d} = \min[d, C_{\mathrm{DES}} \cdot \max(\Delta x_i)] \tag{33}$$

This application of an upper bound to d proportional to the maximum local grid spacing reduces the level of eddy viscosity accordingly at a location away from the wall. This triggers fluctuations at scale proportional to the grid spacing in the flow.

E. Wall-Layer Model for Large-Eddy Simulation

A wall model is necessary to improve the coarse grid representation of LES near the wall. Unlike the formulation of the other approaches, the wall-layer model is best represented in a body-fitted coordinate $(\xi,\ \eta,\ \zeta)$, where η is the wall-normal coordinate. Specifically, tangential wall stresses are correlated with the instantaneous velocities at the first point normal to the wall,[32]

$$\tau_{\eta\xi,w} = [\langle\tau_w\rangle/\langle V_s(\xi,\eta_1,\zeta)\rangle]v_s^\xi(\xi,\eta_1,\zeta) \tag{34}$$

$$\tau_{\eta\zeta,w} = [\langle\tau_w\rangle/\langle V_s(\xi,\eta_1,\zeta)\rangle]v_s^\zeta(\xi,\eta_1,\zeta) \tag{35}$$

where angle brackets denote an averaging over the homogeneous directions and η_1 is the first point in the direction normal to the wall. $\langle V_s\rangle$ is the averaged streamwise velocity over the homogeneous direction at the first point above the wall, while v_s^ξ and v_s^ζ are its instantaneous components in the wall parallel directions. The model for $\langle\tau_w\rangle$ is derived from a simplification of the boundary-layer equation. Omitting the averaging operator notation for simplicity, the averaged wall stress is modeled by[33]

$$\tau_w = [(\mu+\mu_t)\partial_\eta u]_Y - Y\frac{dp}{d\xi} \tag{36}$$

where Y is the distance of a reference point, located in the logarithmic layer, to the wall, and p is the static pressure at the wall. The first term is modeled by the universal log law, which is equivalent to substituting μ_t with the Prandtl mixing length model. The intercept of the log law decreases as a function of surface roughness. The second term in Eq. (36) models the effect of pressure gradient. Hence, this equation in effect constitutes a wall stress model that takes into account the effects of pressure gradient and surface roughness. The wall stress components in the body-fitted system are then inversely transformed to the Cartesian system.

F. Heat Transfer

Once the wall stress is provided through either the wall-layer model, RANS, DES, or full LES, the heat transfer is derived through the Reynolds analogy. Specifically, the relation between Stanton number S_t, which is a measure of wall heat transfer, and skin friction can be expressed as[34]

$$S_t\Big/\tfrac{1}{2}C_f = Pr_t^{-0.66} \approx 1 \tag{37}$$

where Pr_t is the turbulent Prandtl number. The wall heat transfer rate follows directly from the definition of Stanton number and skin friction in the preceding equation, which results in

$$\dot{q}_w = \tau_w C_p(T_w - T_e)/u_e \tag{38}$$

where τ_w is the wall stress and C_p is the same specific heat used in general heat flux equation (7); T_e and u_e are the temperature and streamwise velocity at the edge of the boundary layer, respectively.

IV. Results and Discussion

In this section results of several test cases are presented. Specifically, LES validation in CPR and O86, and wall-layer model (WLM) validation in channel flow are discussed. The application of LES in predicting the effect of inhibitors is also presented.

A. Compressible Periodic Rocket

The domain size of the CPR test case is $2\pi h \times h \times \pi h$, where $h = 0.01$ m is the half-channel height, the same as the height of the rocket chamber in the O86 case discussed later. We perform LES of CPR at the injection Reynolds numbers 190 and 7840 using grid resolution $95 \times 95 \times 47$ and $95 \times 65 \times 33$, respectively, and compare the results with the direct numerical simulation (DNS) data of Venugopal[1] corresponding to the lower injection Reynolds number. The DNS was performed using a Fourier spectral representation in the periodic directions with 384 quadrature points, and B-splines in the wall-normal direction with 192 collocation points. For the LES we use the second-order finite volume method described briefly in Sec. III. The ratio of the LES basic filter width to the grid spacing is 2. The injection mass rate is fixed at 13 kg/(m$^2 \cdot$ s) and injection temperature at 260 K. The injection to bulk mass flux ratio ϵ is 0.025, corresponding to the turbulent regime of the O86 case.

Figure 5 shows the near-wall streaks of the two cases at the same plane parallel from the wall. The streaks represent the isosurface of positive and negative streamwise velocity fluctuations. The resolved streak structures are much more isotropic than those in turbulent channel flows without injection. The high-Reynolds-number streaks are only slightly more diffused compared to their low-Reynolds-number counterpart, which is the result of the subgrid representation in LES. The average streak width in the high-Reynolds-number case is in fact comparable to the filter width. The mean flow comparison can be seen in Fig. 6 for the streamwise and wall-normal momenta, local Mach number, density, and temperature, respectively. The Mach-number profile is presented in the same subplot as the wall-normal momentum. Both high-(dash-dot) and low- (dash) Reynolds-number LES mean flows are in very close agreement with the DNS data. The close agreement indicates the insignificant effect of Reynolds number on the mean flow. The overall mean flow result also suggests the grid insensitivity of LES, because a finer grid is used in the low-Reynolds-number case. The Reynolds number effect appears, however, when we observe the turbulence statistics, as presented in the rms comparison of density fluctuations in Fig. 7 and turbulence intensity in Fig. 8. The results of the higher Reynolds number LES show a shift toward the injection wall similar to that observed in turbulent channel flow. The LES model contribution is higher in the high-Reynolds-number case, which can be seen in Fig. 9, where the model coefficient C_d and turbulent (as well as laminar) viscosity are shown in the top two panels. The level of eddy viscosity is comparable to the molecular viscosity in the low-Reynolds-number case (solid lines). In the high-Reynolds-number case, the ratio of eddy to molecular viscosity is significantly higher (dashed lines). The SGS model is thus essential in the high-Reynolds-number case to compensate for the low grid resolution. Indeed, without employing the SGS model, the high-Reynolds-number simulation is unstable due to the absence of artificial dissipation. The relative difference between the two Reynolds numbers is approximately the same for C_d and μ_t. This indicates that the magnitude of the strain rate is comparable

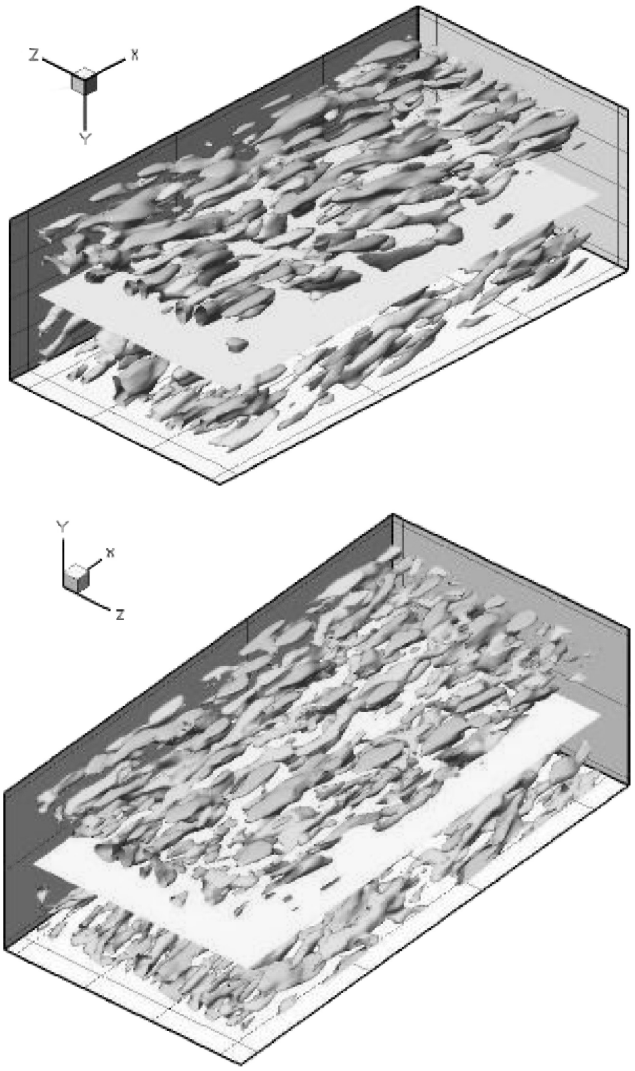

Fig. 5 Near-wall streaks of CPR at $Re_{inj} = 190$ (top) and $Re_{inj} = 7840$ (bottom) with purple representing positive u' and green negative.

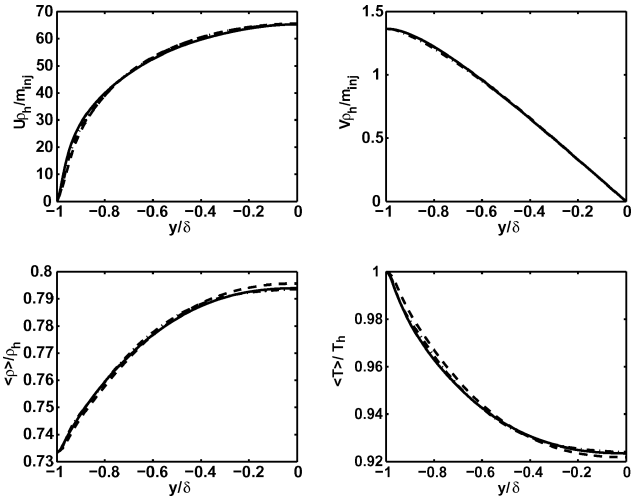

Fig. 6 Mean flow comparison in streamwise momentum, wall-normal momentum, and local Mach number, density, and temperature in wall-normal direction, respectively, between DNS at $Re_{inj} = 190$ (solid lines), LES at $Re_{inj} = 190$ (dashed lines), and LES at $Re_{inj} = 7840$ (dash-dotted lines).

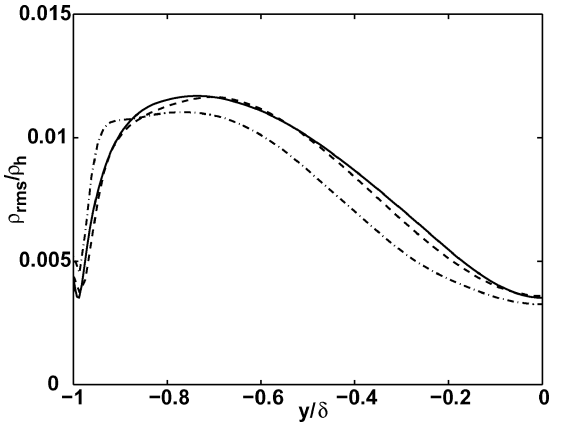

Fig. 7 RMS of density fluctuations nondimensionalized by head-end density: DNS at $Re_{inj} = 190$ (solid line), LES at $Re_{inj} = 190$ (dashed line), and LES at Re_{inj} =7840 (dash-dotted line).

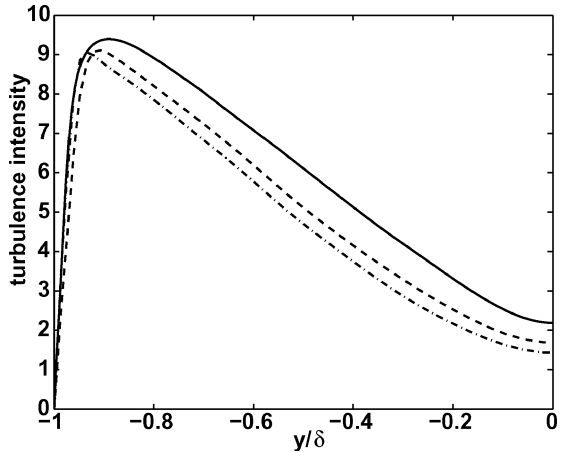

Fig. 8 Same comparison as previous figure for turbulence intensity nondimensionalized by injection velocity.

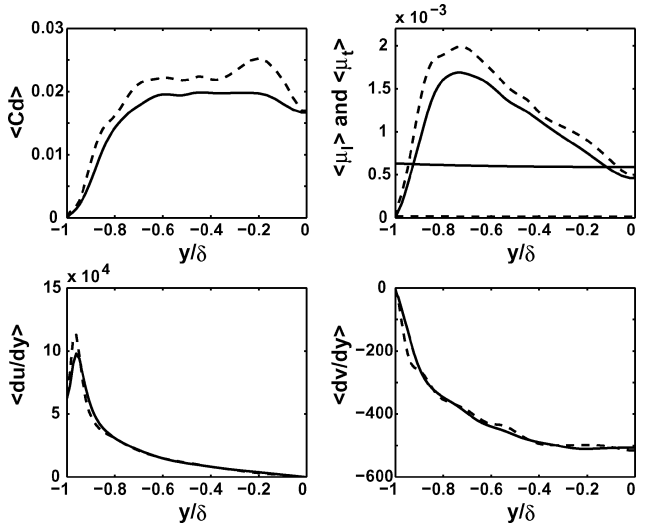

Fig. 9 Comparison in dynamic model coefficient, molecular and turbulent viscosity, du/dy, and dv/dy in wall-normal direction, respectively, between LES at $Re_{\text{inj}} = 190$ (solid lines) and LES at $Re_{\text{inj}} = 7840$ (dashed lines).

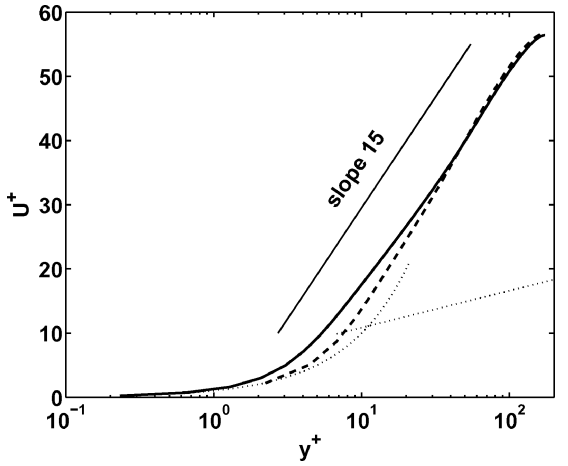

Fig. 10 CPR streamwise velocity profile in wall units at $Re_{\text{inj}} = 190$: DNS (bold solid line), LES (dashed line), universal log-law (dotted line), and du^+/d$y^+ = 15$ (thin solid line).

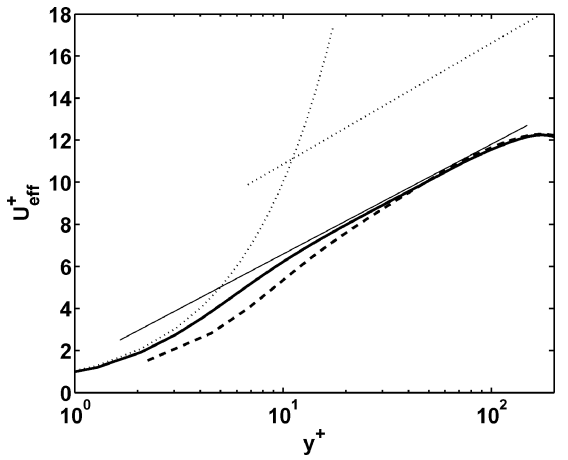

Fig. 11 Similar to preceding figure for effective streamwise velocity profile: DNS (bold solid line), LES (dashed line), universal log-law (dotted lines), and $u^+ = 2.27\ln(y^+) + 1.75$ (thin solid line).

in the high- and low-Reynolds-number cases, based on the eddy viscosity principle followed in the SGS modeling. This observation appears to be consistent with the structures of turbulence near the wall shown in Fig. 5. Higher strain rates would have resulted in more elongated streaks. The bottom two panels of Fig. 9 show the slope of the streamwise and normal velocities, respectively, in the wall-normal direction. The different Reynolds numbers exhibit nearly the same slopes. The slope of the normal velocity component is negative throughout the cross section and monotonically decreasing. It reaches the minimum value at the centerline. The local maximum in the streamwise velocity slope located near the wall indicates an inflection point in the velocity profile. The existence of inflection point has also been reported by Nicoud et al.[15] and Venugopal.[1] This inflection point is a consequence of the wall injection and causes injection-driven flows to be inviscidly unstable. The higher the injection to bulk mass flux ratio ϵ, the farther away from the wall the inflection point would be.

To perform a more critical assessment of the mean flow profiles near the injection wall, we plot on a logarithmic scale the mean streamwise velocity profiles in wall units for the case with an injection Reynolds number of 190. This is presented in Fig. 10. Using the DNS of Venugopal[1] as a reference, it is shown that LES underpredicts the velocity profile very close to the wall. This indicates that the near-wall solution is underresolved; in other words, the injecting wall places a restriction on the grid resolution, though not as severe as at a noninjecting wall. Compared to the universal log- law of a noninjecting wall, the laminar sublayer is valid for $y^+ < 2$, whereas the buffer layer is completely absent. The profiles above $y^+ = 10$ resemble a logarithmic function of y^+ with a much higher slope (approximately 15) than $1/\kappa$, where κ is the von Kármán constant. This value of logarithmic slope is also found in the numerical study of Nicoud et al.[15] The mass flux ratio in their study ($\epsilon = 0.029$) is comparable to the value in the present study ($\epsilon = 0.025$). The higher velocity in wall units is a consequence of the low wall stress and, thus, friction velocity due to the injection. The skin friction value is accordingly lower than at the canonical boundary layer. When expressed as the effective velocity in wall units,[15,35,36]

$$u^+_{\text{eff}} = \left(2/v^+_{\text{inj}}\right)\left[\sqrt{1 + v^+_{\text{inj}} u^+} - 1\right] \approx (1/\kappa) ln(y^+) + C\left(v^+_{\text{inj}}\right) \quad (39)$$

we found that the logarithmic slope and the intercept fit best with 2.27 (rather than $1/\kappa \approx 2.5$) and 1.7, respectively. This is shown in Fig. 11. Using the effective velocity, the buffer layer is weakly present and located closer to the wall compared to the universal log- law (dotted lines). The logarithmic line of the injection case is represented by the thin solid line. The effect of injection is clearly the decrease of the intercept, which has been reported by previous investigators.[15,37,38] Similar to the previous figure, the result from LES underpredicts the buffer region but exhibits a close agreement with DNS in the logarithmic region.

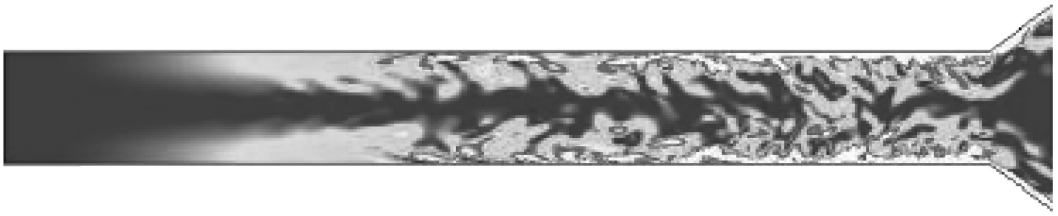

Fig. 12 Total vorticity contours of O86 case using LES dynamic Smagorinsky.

B. O86 Case

The dimension of the simulated laboratory-scale rocket mimics the experimental apparatus of Traineau et al.'s cold flow measurements.[14] Specifically, the axial extent of the laboratory-scale rocket is 48 times the half-chamber height without the nozzle and 51.2 times with the nozzle. The spanwise dimension is twice the chamber height. The same physical parameters and boundary conditions are also employed in the present study. To imitate the injection through the porous wall, a mass injection boundary condition is imposed and random fluctuations with specified amplitude are added to trigger and sustain the three-dimensionality of the flow. The flow domain in the O86 chamber can be divided into a laminar regime near the head end, a turbulent regime in the aft part near the nozzle, and a transition regime in between, as shown by the vorticity contours in Fig. 12. The transition regime is characterized by backward-inclined vortices, as also observed in the linear regime solution of the CPR case.[1] This injection-driven transitional flow is new territory for LES. This flow case has been used as a reference test case by many researchers: among others, Apte and Yang.[13] The finest grid resolution we use, however, is an order of magnitude lower compared to that of Apte and Yang. Because LES is supposedly grid independent provided that the resolution is sufficient, the present case also forms a more stringent test to the subgrid model used.

Two LES cases with different resolutions were conducted. The first resolution is $210 \times 65 \times 33$ in the streamwise, normal, and spanwise directions, respectively, whereas the second resolution is finer by a factor of 2 in the streamwise direction. In addition, the finer grid has a higher stretching ratio in the wall-normal direction so that the normal spacings near the wall are smaller, whereas the coarse grid is more uniform in the normal direction but clustered axially in the turbulent region. The amplitude of the injection mass rate fluctuations at the walls is 5% of the mean value. The filter width ratio, defined as the ratio of the basic filter width to the local grid spacing, is 1 for the coarse case and 2 for the finer case. The reason for the difference is merely to compensate for the difference in the spacing due to different resolutions. With lower ratio one tries to resolve smaller eddys, that is, of the size of local grid spacing in the coarse grid case, which is comparable to twice the spacings in each coordinate direction of the finer grid. Therefore, the filter width ratio of 2 is used in the finer grid case.

The evolution of the axial velocity profiles from the laminar to the turbulent state is depicted in Fig. 13. The figure compares the two LES cases against Traineau's data.[14] The compressible theoretical solution of Balakrishnan et al.[3] is included to indicate the effect of turbulence. At $x/h = 3.45$, the LES cases and the measurement data collapse to the compressible laminar profile, which is virtually the same as Taylor's profile because the compressibility effect is negligible near the head end. At the transition and turbulent locations, $x/h = 33.0$ and 47.0, respectively; the effect of turbulence is clearly seen from the more convex profile of the experiment compared to the laminar theory. The coarse-grid LES overpredicts the velocity profiles from experiment at these locations, whereas the fine-grid LES produces a much closer agreement.

To assess the turbulence prediction of the LES approach, we compare the second moment variables, as represented by the shear stress comparison in Fig. 14, at five axial locations. No artificial dissipation is employed in order to avoid uncertainty due to the interference with the physical dissipation. Spurious numerical residuals are controlled

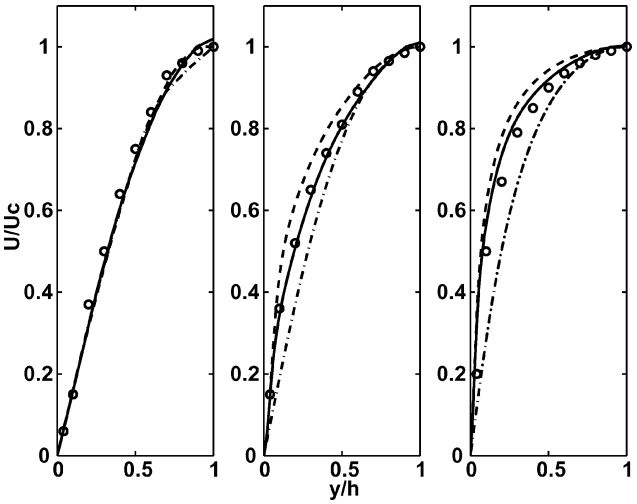

Fig. 13 Streamwise velocity profiles normal to injection wall at axial locations $x/h = 3.45$, 33.01, and 47.00: measurement data by Traineau et al.[14] (circles) compared to fine-grid LES (solid lines) and coarse-grid LES (dashed lines). Profiles from laminar compressible theory are included (dash-dotted lines).

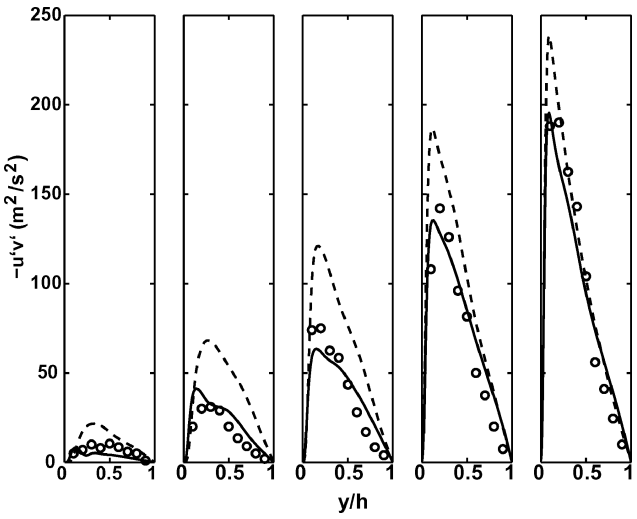

Fig. 14 Shear stress profiles normal to injection wall at axial locations $x/h = 14.99$, 24.00, 30.13, 40.46, and 45.97: measurement data by Traineau et al.[14] (circles) compared to fine-grid LES (solid lines) and coarse-grid LES (dashed lines).

merely through the grid manipulation (refinement and stretching). The physical source of turbulence comes from the wall-injection fluctuations. The earlier start of transition in the coarse-grid LES is apparently due to the large disturbances in the laminar region caused by a combination of the injection fluctuations and the numerical errors. As a result, the turbulent stress is overpredicted throughout the transition region. The measured stress level at $x/h = 30$ has been nearly reached by the coarse-grid LES at $x/h = 24$. The fine-grid LES, on the other hand, maintains the disturbances in the laminar

region at about the same level as the pseudoturbulence in the experiment. The level and profile of the turbulent stresses in the fine-grid case are in close agreement with the experiment. The overprediction of the coarse-grid case is, however, reduced when the flow enters the turbulent regime. A similar assessment holds for the turbulence intensity shown in Fig. 15.

The dynamic LES is obviously more sensitive to the grid when applied to transitional flow compared to fully turbulent flow, such as in the CPR case. The negligible viscous effect of the injection-driven flow does not completely remove the restriction associated with the grid resolution. The subgrid representation of disturbances in the transition region is more challenging than that in the turbulent region due to the anisotropic character of these disturbances. Hence, adequate resolution is needed to capture the disturbances in the transition region rather than relying on the subgrid representation. Nevertheless, as far as the mean and the second moment statistics are concerned, the current results are comparable to the results of Apte and Yang[13] despite a much coarser grid used in the present simulation.

C. O86i Case

In the O86i case, an inhibitor is mounted to the top and bottom walls in the laminar region at approximately $x/h = 12$. Figure 16 shows the isosurface of spanwise vorticities in the O86i simulation. Compared to the case without inhibitors, the rolled up vortices are lifted farther from the wall due to the presence of the inhibitors. The shed vortex structures have higher circulation, which contributes to a higher turbulent stress in the region downstream of the inhibitor, as can be seen in Fig. 17. In this figure, the turbulent stress of the clean O86 (dash-dotted lines) is compared to that of O86i with 50% injection perturbation (dashed lines) and O86i with uniform injection (solid lines). In addition to the increase in turbulence level caused by the obstacles, the turbulent stresses of O86i with and without injection perturbations are virtually the same. This suggests that the injection-induced turbulence from the propellant surface is overshadowed by the geometry-induced turbulence. The inhibitor functions as a trip, bypassing the natural transition. Although this may suggest that accurate modeling of injection turbulence is less crucial during the steady burning of the propellant, it remains indispensable during the ignition process when the inhibitors do not

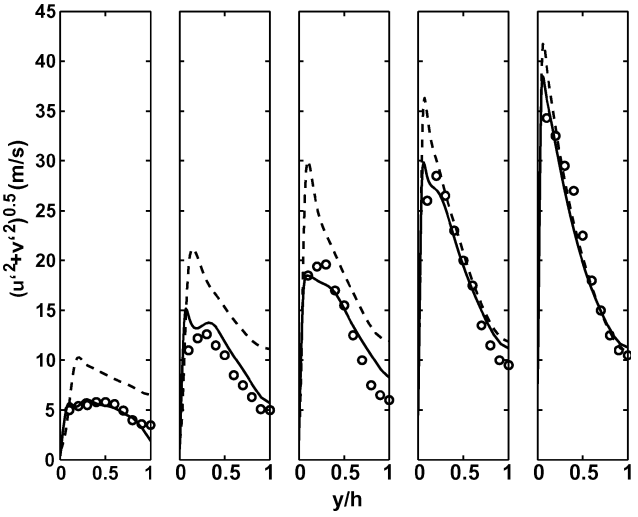

Fig. 15 Turbulence intensity profiles normal to injection wall at axial locations x/h = 14.99, 24.00, 30.13, 40.46, and 45.97: measurement data by Traineau et al.[14] (circles) compared to fine-grid LES (solid lines) and coarse-grid LES (dashed lines).

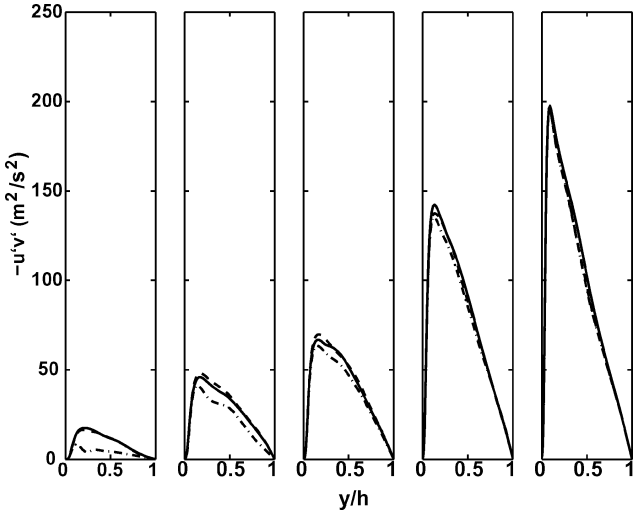

Fig. 17 Comparison of turbulent stresses from LES of O86 between smooth case with injection fluctuations (dash-dotted lines), inhibitor case with 50% fluctuations (dashed lines) and inhibitor case with uniform injection (no fluctuations; solid lines).

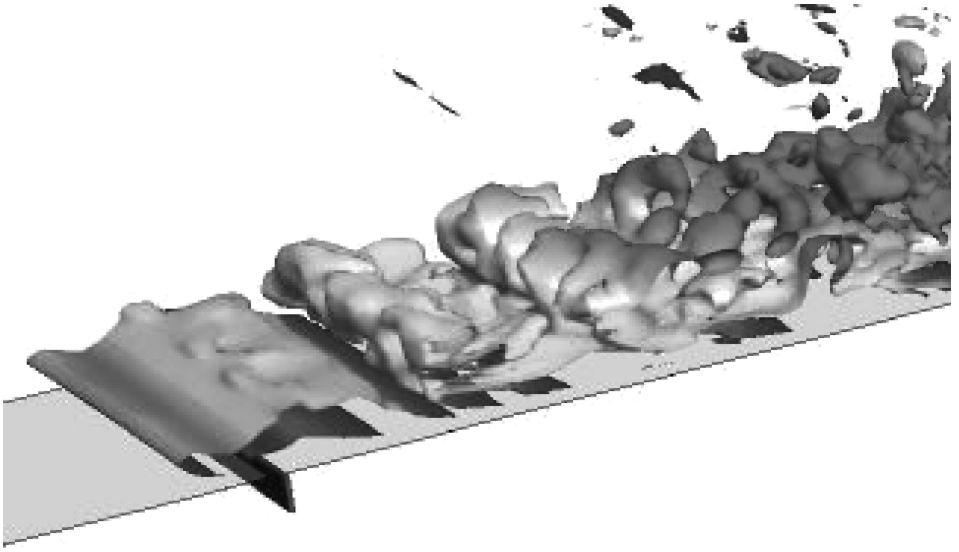

Fig. 16 Total vorticity isosurface of O86i using LES dynamic Smagorinsky.

protrude into the flow. Even during the propellant burning, the first segment near the head end is not affected by the inhibitors. The injection turbulence is more important in this region.

A proper modeling of injection turbulence encounters the problem of scale disparity between the gas fluctuations coming from the combustion surface and the resolved scale of the fluid (LES) simulation. The fluctuation length scale at the combustion level is on the order of tens of microns while the resolved fluid scale in a full-scale simulation is on the order of a centimeter. Modeling subgrid effects of the combustion fluctuations would require a direct simulation in the small scales to characterize the distribution function of the large scales. The latter is then used for the inflow condition in LES.

D. Wall-Layer Model

This subsection is concerned with the validation of wall models for the nozzle thin boundary layer, illustrated by the dark layer along the nozzle wall in Fig. 2. The selection of WLMs is based on a simple cost–benefit analysis, that is, weighing the cost increase against the physical and computational features carried by the model. The additional cost due to the inclusion of a wall model to a coarse-grid LES is simply given by the following expression:

$$\Delta\text{cost} = c_{\text{ps}}(R_N R_{\text{work}}/R_{\text{dt}}) \tag{40}$$

where c_{ps} is the problem size ratio between the nozzle and the whole rocket chamber, assumed to be the grid size ratio, typically about 0.1 for the Titan and reusable SRM simulations. For example, if the whole fluid domain of the rocket is meshed by 2 million points, 0.2 million are devoted to the nozzle domain. R_N is a multiplication factor due to the increase in grid points required by the attached model. Similarly, R_{work} is a multiplication factor due to the increase in work per grid cell, estimated from the additional equations to be solved assuming consistency in the numerical method used. $R_{\text{dt}} < 1$ denotes the time step ratio due to the decrease in dt. R_N, R_{work}, and R_{dt} are functions on the wall model.

The list of wall models considered for implementation is shown in Table 2 along with the estimated cost increase and the physical and computational features of each model. The cost estimation is based on injection Reynolds number of about 8000 in a typical laboratory-scale rocket. It is assumed that implicit time discretization is used; otherwise, the cost increase would be much larger due to the reduction in R_{dt}. Transforming to the bulk Reynolds number using a typical injection mass flux ratio near the nozzle inlet, $\epsilon = 0.025$, gives $Re_b \approx 320{,}000$ or $Re_\tau \approx 16{,}000$, which would rise to $Re_\tau \approx 48000$ at the nozzle outlet assuming no boundary-layer separation and an increase in Mach number by a factor of 3. Obviously, Re_τ would increase with increasing injection mass rate, rocket size, and flow acceleration in the nozzle. Using DES for the entire domain of the nozzle instead of coarse-grid LES, for instance, does not increase the computational cost in spite of the increase in the wall-normal grid points to satisfy the DES grid-making policy.[16] In the O86 case considered as a coarse-grid LES earlier, 64 cells are employed in the wall-normal direction. Increasing it by 2.5 times to 160 would be sufficient to capture the thin nozzle boundary layers (60 for the core and 50 for each boundary layer), considering that $Re_\tau = 20{,}000$ in channel flow can be achieved using 90 points in the wall-normal direction as demonstrated by Nikitin et al..[16] On the other hand, DES is about 2.5 times cheaper per grid point than the dynamic LES. The additional cost is, hence, negligible. In model 2, we apply DES in the wall region as a wall model of LES. In the same way, the other models are attached to LES. The same cost analysis suggests the values depicted in the table. The WLM in model 5 is based on the model described in Sec. III.

A full-scale rocket diameter could be 200 times larger than the laboratory scale considered here. It is nevertheless still attractive to use a resolved wall model such as DES in such a full-scale simulation. As suggested by Nikitin et al.,[16] an increase by a factor of 10 in Re_τ using DES adds only 17 cells for each wall, based on the wall-normal stretching ratio of 1.15, which is typical for DES. The increase of grid points in the wall-normal direction thus scales logarithmically with the Reynolds number. This implies that, assuming an increase in Re_τ by a factor of 200, adding another 38 cells (to the existing 50) for each wall is sufficient to promote a laboratory-scale DES to a full-scale one in addition to the core flow refinement. It should be noted that a nonconforming grid capability is required to allow zonal grid refinement.

The aim of wall modeling is to provide approximate wall stress and heat transfer. The table indicates physical features that can be taken into account by each model. Based on the cost and the features potentially covered, we implement models 1, 2, and 5 in our code. It is essential that the model accounts for the effects of pressure gradient, surface roughness, stagnation, and external forces due to acceleration and rotation in a lifting rocket. The two-layer model (TLM) of Balaras et al.[39] is based on solving the boundary-layer equations in the wall layer using a simple turbulence model for the eddy viscosity. Although compelling, the model is not practical if applied to complex flows due to the need for solving a different type of equation in the inner layer on an embedded mesh. For similar computational reasons, integral boundary-layer methods are less suitable because the marching procedure required by the parabolic system does not permit parallel processings in the streamwise direction. The most important limitation of the boundary-layer approach is, however, its basic assumption that the interaction between the inner and the outer layers is weak. This assumption is in general invalid for nozzle flows where separation and shock boundary-layer interaction commonly occur.

We performed verification of models 1 and 5 in a plane channel flow. As can be seen in the plot of logarithmic profiles in Fig. 18, five test cases are considered, namely, full LES at $Re_\tau = 180$, LES + WLM at $Re_\tau = 1000$ and $Re_\tau = 3000$, DES at $Re_\tau = 2000$, and RANS–SA at $Re_\tau = 3000$. The dimension for all cases is $2\pi h \times 2h \times \pi h$, in the streamwise, wall-normal, and spanwise directions,

Table 2 Comparison of additional cost and physical and computational features or deficiencies covered by various wall models attached to LES[a]

Model attached	Cost increase (implicit)	Features covered[b]
1. DES whole nozzle	0%	PG, SR, ACC, STG, ROT, 1GRD, PARAL
2. DES	7%	PG, SR, ACC, STG, ROT, 1GRD, PARAL
3. TLM-RANS	7%	PG, SR, ACC, STG, ROT, 2GRD, PARAL
4. TLM-BL	2%	PG, SR, 2GRD, SERI
5. WLM	1%	PG, SR, 1GRD, PARAL
6. BL integral method	1%	PG, SR, 1GRD, SERI

[a]The estimated cost increase is based on a laboratory scale rocket.
[b]BL, boundary layer; PG, pressure gradient; SR, surface roughness; ACC, acceleration; STG, stagnation; ROT, rotation; 1GRD, one-grid system; 2GRD, two-grid system; PARAL, parallelable; SERI, only serial.

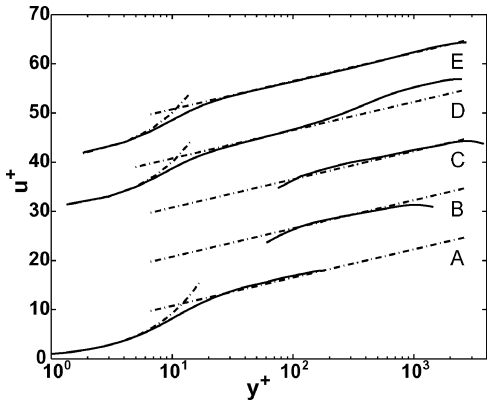

Fig. 18 Channel flow logarithmic profiles of LES $Re_\tau = 180$ (case A), LES + WLM $Re_\tau = 1000$ (case B), LES + WLM $Re_\tau = 3000$ (case C), DES $Re_\tau = 2000$ (case D), and RANS–SA $Re_\tau = 3000$ (case E).

respectively, except for case A, which employs $2\pi h \times 2h \times 4/3\pi h$, with $h = 0.01$ m. The grid size for case A is $64 \times 128 \times 64$, whereas for the high-Reynolds-number cases it is $64 \times 64 \times 32$. The bulk velocity is equivalent to a bulk Mach number of 0.5, implying low compressibility effect. The low-Reynolds-number LES, case A, captures the universal log law accurately. LES+WLM at $Re_\tau = 1000$ and 3000, cases B and C, are in reasonable agreement with the theory. We observe that the slope of case C deviates slightly and this trend continues at Reynolds numbers above $Re_\tau = 3000$, indicating the need to increase the grid resolution. Case D, which is DES at $Re_\tau = 2000$, produces an adjustment in the log profile typical for DES of channel flow.[16] This manifests in a higher intercept in the LES region, which implies underprediction of the skin friction. DES can, however, be applied at much higher Reynolds numbers without a severe penalty in grid size. Case E, RANS at $Re_\tau = 3000$, aligns with the theory, as expected.

We computed an additional case not included in Fig. 18, namely coarse-grid LES without WLM at $Re_\tau = 1000$, for convenience called case F. The rms values of streamwise and wall-normal velocity fluctuations, normalized by the friction velocity, are shown in Figs. 19 and 20, respectively. In these figures B and F are compared with the DNS data of del Alamo et al.[40] at $Re_\tau = 950$. Figure 19 shows that the level of the near-wall peaks in u fluctuations in case B are comparable to those of the DNS data, thanks to the WLM. The fluctuation level away from the wall is, however, underestimated by the simulation using WLM. Case F, on the other hand, overestimates the rms values by a factor of nearly 2 near the wall, although this is less severe in the core region. This overestimation is due to

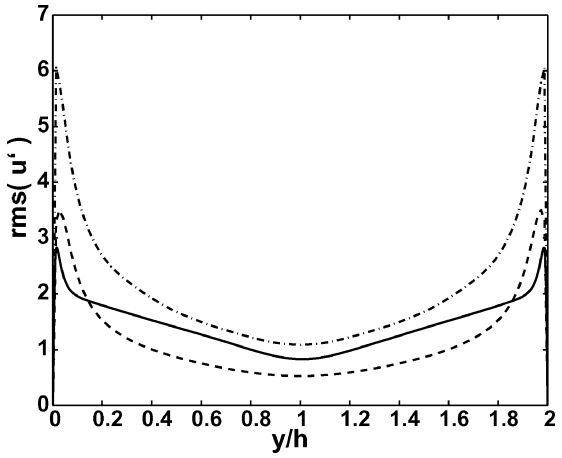

Fig. 19 RMS of streamwise velocity fluctuations of DNS $Re_\tau = 950$ (solid line), LES + WLM $Re_\tau = 1000$ (dashed line), LES $Re_\tau = 1000$ (without wall model; dash-dotted line).

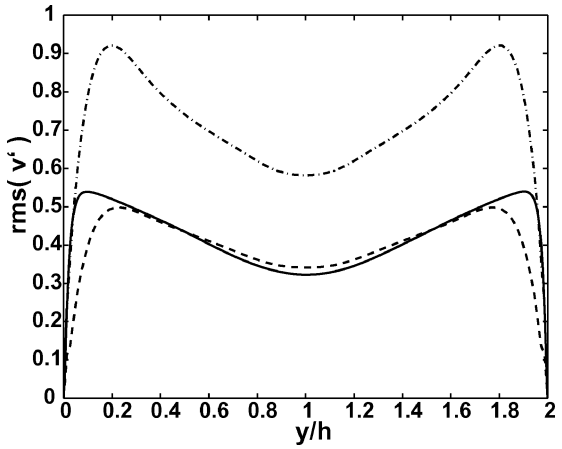

Fig. 20 Same comparison as previous figure for RMS of wall-normal velocity fluctuations.

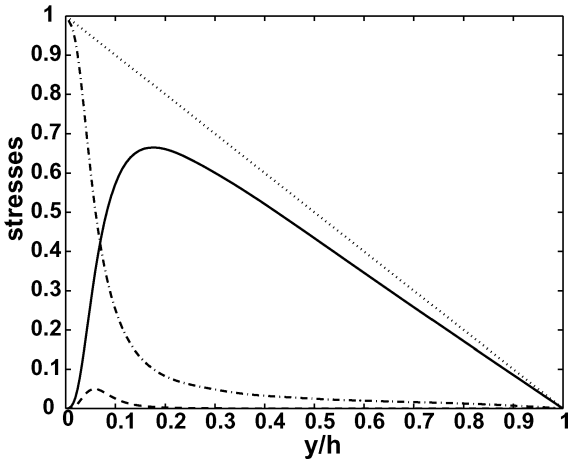

Fig. 21 Stress components of DES $Re_\tau = 180$: resolved (solid line), model (dashed line), viscous (dash-dotted line), and total (dotted line).

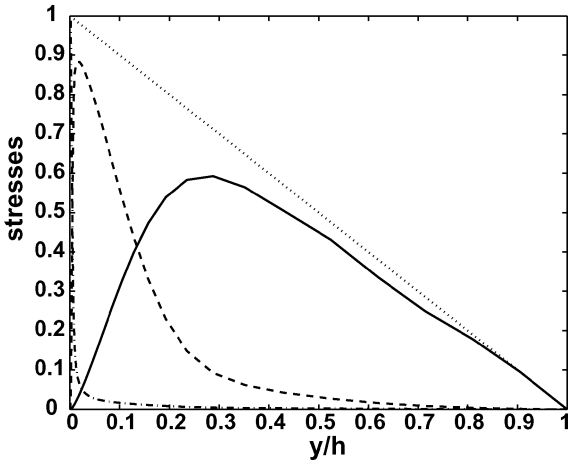

Fig. 22 Similar to previous figure for DES $Re_\tau = 3000$ case.

the underprediction of the skin friction or, equivalently, the friction velocity that is used for the normalization of the rms quantities. A similar result is shown for the rms of wall-normal fluctuations in Fig. 20. The LES using WLM is in close agreement with DNS. The near-wall peaks are, however, located farther from the walls compared to DNS. Case F, on the other hand, significantly overestimates the rms value throughout the channel cross section.

Figures 21 and 22 show the stress components of DES at $Re_\tau = 180$, which is virtually the same as LES at the same Reynolds number (case A), and DES at $Re_\tau = 3000$ (case D), respectively. Comparing these figures, the model contribution of DES becomes more dominant with the increasing Reynolds number. The opposite holds for the viscous contribution, whereas the resolved components are comparable between the two cases. We obtain qualitatively the same DES result as in the incompressible counterpart reported by Nikitin et al.[16] It was found that using second-order central discretization for the turbulence model equation yields a better result than first-order upwind. In contrast to the incompressible DES, where a semi-implicit method is used, we employ a four stage Runge–Kutta scheme for both Navier–Stokes and Spalart–Allmaras equations in this study. A multistage explicit scheme is used for the steady-state calculation of the fully RANS case, such as case E. Further investigation is needed on the time discretization of DES, including consideration of a dual time-stepping method.

V. Conclusions

The complexity of validating the SRM internal flow simulation is reduced by dividing it into simplified problems that can be studied

individually in a more rigorous way. Various test cases and tools are outlined systematically to tackle a broad range of modeling and validation tasks.

LES results of the CPR case show insensitivity to Reynolds number and, hence, viscous effects. In this fully turbulent flow, LES is also much less sensitive to the grid resolution compared to wall-bounded flows without injection and transitional flows. We found similar findings to those of Nicoud et al.[15] at comparable injection ratio and Reynolds number, despite the difference in specification of the upper boundary condition and the source terms of the governing flow equations. The effects caused by these differences apparently cancel each other, in that the freestream boundary condition used by Nicoud et al. replaces the role of the mass source term in the present study. The latter is, however, more consistent with the practical rocket application.

In the study of the O86 transitional flow, it is found that adequate resolution, which nevertheless is an order of magnitude lower than Apte and Yang's,[13] is required to capture the disturbances in laminar and transition regions for which the SGS model is not suitable. A fully coarse-grid LES simulation is therefore handicapped by this issue. Understanding the nature of anisotropic disturbances, especially in the laminar region, is necessary to force realistic perturbations explicitly. This can be achieved through better understanding of the nature of injection turbulence, the acoustic instability, and the effect of instability coming from the head-end wall boundary layer, in addition to the known hydrodinamic instability. Turbulence generated by inhibitors overshadows that from the injection fluctuations. Realistic modeling of injection turbulence, however, remains important because the inhibitors do not protrude at ignition.

In modeling the nozzle flow, although DES is a compelling tool due to its lower resolution and computational demand, LES is still prefered for the core region of the nozzle. This is due to the fact that modeling multiphase effects, such as the presence of particles, can be achieved more rigorously through the subgrid modeling in LES. This approach will be more difficult to pursue in DES because the SGS component of DES is conventionally not derived from the filtered system of flow equations. For this reason an interface model is desired that can naturally match DES near the wall to the conventional LES away from the wall. This aspect of modeling will be addressed in the future.

Finally, the fully RANS approach is considered suitable for a first-order estimate of the nozzle wall heat and momentum transfer due to its low computational effort, especially during the steady burning when the statistical properties of turbulence can be better modeled. This information can serve as an approximate wall boundary condition for the corresponding time-accurate simulation.

Acknowledgment

The Center for Simulation of Advanced Rockets is supported by the U.S. Department of Energy through the University of California under subcontract number B341494.

References

[1]Venugopal, P., "Direct Numerical Simulation of Turbulence in a Model Solid Rocket Motor," Ph.D. Dissertation, Univ. of Illinois at Urbana–Champaign, Urbana, IL, 2003.

[2]Taylor, G. I., "Fluid Flow in Regions Bounded by Porous Surfaces," *Proceedings of the Royal Society of London, Series A: Mathematical and Physical Sciences*, Vol. 234, 1956, pp. 456–475.

[3]Balakrishnan, G., Linan, A., and Williams, F. A., "Compressibility Effects in Thin Channels with Injection," *AIAA Journal*, Vol. 29, No. 12, 1991, pp. 2149–2154.

[4]Flandro, G. A., "Effects of Vorticity on Rocket Combustion Stability," *Journal of Propulsion and Power*, Vol. 11, No. 4, 1995, pp. 607–625.

[5]Flandro, G. A., "On Flow Turning," AIAA Paper 95-2730, July 1995.

[6]Majdalani, J., and Van Moorhem, W. K., "Improved Time-Dependent Flowfield Solution for Solid Rocket Motors," *AIAA Journal*, Vol. 36, No. 2, 1998, pp. 241–248.

[7]Wasistho, B., Balachandar, S., and Moser, R. D., "Compressible Wall-Injection Flows in Laminar, Transitional, and Turbulent Regimes: Numerical Prediction," *Journal of Spacecraft and Rockets*, Vol. 41, No. 6, 2004, pp. 915–924.

[8]Beddini, R. A., "Injection-Induced Flows in Porous-Walled Ducts," *AIAA Journal*, Vol. 24, No. 11, 1986, pp. 1766–1773.

[9]Sabnis, J. S., Gibeling, H. J., and McDonald, H., "Navier–Stokes Analysis of Solid Propellant Rocket Motor Internal Flows," *Journal of Propulsion and Power*, Vol. 5, No. 6, 1989, pp. 657–664.

[10]Chaouat, B., and Schiestel, R., "Reynolds Stress Transport Modelling for Steady and Unsteady Channel Flows with Wall Injection," *Journal of Turbulence*, Vol. 3, No. 21, 2002, pp. 21–21(1).

[11]Liou, T. M., Lien, W. Y., and Hwang, P. W., "Transition Characteristics of Flowfield in a Simulated Solid-Rocket Moter," *Journal of Propulsion and Power*, Vol. 14, No. 3, 1998, pp. 282–289.

[12]Apte, S. V., and Yang, V., "Unsteady Flow Evolution in a Porous Chamber with Surface Mass Injection, II: Acoustic Excitation," *AIAA Journal*, Vol. 40, No. 2, 2002, pp. 244–253.

[13]Apte, S. V., and Yang, V., "A Large-Eddy Simulation Study of Transition and Flow Instability in a Porous-Walled Chamber with Mass Injection," *Journal of Fluid Mechanics*, Vol. 477, 2003, pp. 215–225.

[14]Traineau, J. C., Hervat, P., and Kuentzmann, P., "Cold Flow Simulation of a Two Dimensional Nozzleless Solid Rocket Motor," AIAA Paper 86-1447, June 1986.

[15]Nicoud, F. C., Poinsot, T. J., and Ha Minh, H., "Direct Numerical Simulation of Turbulent Flow with Massive Uniform Injection," *Proceedings of the 10th Symposium on Turbulent Shear Flows*, Vol. 10, Pennsylvania State Univ., Aug. 1995.

[16]Nikitin, N. V., Nicoud, F., Wasistho, B., Squires, K. D., and Spalart, P. R., "An Approach to Wall Modeling in Large-Eddy Simulation," *Physics of Fluids*, Vol. 12, No. 7, 2000, pp. 1629–1632.

[17]Langford, J. A., and Moser, R. D., "Optimal LES Formulations for Isotropic Turbulence," *Journal of Fluid Mechanics*, Vol. 398, 1999, pp. 321–346.

[18]Dean, R. B., "Reynolds Number Dependence of Skin Friction and Other Bulk Flow Variables in Two-Dimensional Rectangular Duct Flow," *Journal of Fluids Engineering*, Vol. 100, June 1978, pp. 215–223.

[19]Jameson, A., Schmidt, W., and Turkel, E., "Numerical Solutions of the Euler Equations by Finite Volume Methods Using Runge–Kutta Time-Stepping Schemes," AIAA Paper 81-1259, 1981.

[20]Blazek, J., "Flow Simulation in Solid Rocket Motors Using Advanced CFD," AIAA Paper 2003-5111, 2003.

[21]Vreman, A. W., "The Filtering Analog of the Variational Multiscale Method in Large-Eddy Simulation," *Physics of Fluids*, Vol. 15, No. 8, 2003, pp. L61–L64.

[22]Wasistho, B., Geurts, B. J., and Kuerten, J. G. M., "Simulation Techniques for Spatially Evolving Instabilities in Compressible Flow over a Flat Plate," *Computers and Fluids*, Vol. 26, No. 7, 1997, pp. 713–739.

[23]Vreman, B., Geurts, B., and Kuerten, H., "A Priori Test of Large Eddy Simulation of the Compressible Mixing Layer," *Journal of Engineering Mathematics*, Vol. 29, No. 4, 1995, pp. 299–327.

[24]Favre, A., "Turbulence: Space-Time Statistical Properties and Behaviour in Supersonic Flows," *Physics of Fluids A*, Vol. 3, Oct. 1983, pp. 2851–2863.

[25]Vreman, B., Geurts, B., Kuerten, H., Broeze, J., and Wasistho, B., "Dynamic Subgrid-Scale Models for LES of Transitional and Turbulent Compressible Flow in 3-D Shear Layers," *Proceedings of the 10th Symposium on Turbulent Shear Flows*, Vol. 10, Pennsylvania State Univ., 1995, pp. 10.25–30.

[26]Vreman, B., Sandham, N. D., and Luo, K. H., "Compressible Mixing Layer Growth Rate and Turbulence Characteristics," *Journal of Fluid Mechanics*, Vol. 320, 1996, pp. 235–258.

[27]Germano, M., Piomelli, U., Moin, P., and Cabot, W. H., "A Dynamic Subgrid-Scale Eddy Viscosity Model," *Physics of Fluids A*, Vol. 3, 1991, pp. 1760–1765.

[28]Lilly, D. K., "A Proposed Modification of the Germano Subgrid Scale Closure Method," *Physics of Fluids A*, Vol. 4, 1992, pp. 633–635.

[29]Moin, P., Squires, K., Cabot, W., and Lee, S., "A Dynamic Subgrid-Scale Model for Compressible Turbulence and Scalar Transport," *Physics of Fluids A*, Vol. 3, 1991, pp. 2746–2757.

[30]Horiuti, K., "Large Eddy Simulation of Turbulent Channel Flow by One Equation Modeling," *Journal of the Physical Society of Japan*, Vol. 54, 1985, pp. 2855–2865.

[31]Spalart, P. R., and Allmaras, S. R., "A One-Equation Turbulence Model for Aerodynamic Flows," *Recherche Aerospatiale*, No. 1, 1994, pp. 5–21.

[32]Piomelli, U., Ferziger, J., Moin, P., and Kim, J., "New Approximate Boundary Conditions for Large Eddy Simulations of Wall-Bounded Flows," *Physics of Fluids A*, Vol. 1, June 1989, pp. 1061–1068.

[33]Hoffmann, G., and Benocci, C., "Approximate Wall Boundary Conditions for Large Eddy Simulations," Advance in Turbulence V, edited by R. Benzi, Kluwer, Dordrecht, 1995, pp. 222–228.

[34]Schlichting, H., *Boundary Layer Theory*, 7th ed., McGraw–Hill, New York, 1987.

[35]Michel, R., Quemard, C., and Durand, R., "Application d'un schema de logueur de melange I'etude des couches limites turbulentes d'equilibre," Technical Rept., ONERA NT No. 154, 1969.

[36]Simpson, R., "Characteristics of Turbulent Boundary Layers at Low Reynolds Numbers with and Without Transpiration," *Journal of Fluid Mechanics*, Vol. 42, 1970, pp. 769–802.

[37]Piomelli, U., Moin, P., and Ferziger, P., "Large Eddy Simulation of the Flow in Transpired Channel," *Journal of Thermophysics and Heat Transfer*, Vol. 5, No. 1, 1991, pp. 124–128.

[38]Sumitani, Y., and Kasagi, N., "Direct Numerical Simulation of Turbulent Transport with Uniform Wall Injection and Suction," *AIAA Journal*, Vol. 33, No. 7, 1995, pp. 1220–1228.

[39]Balaras, E., Benocci, C., and Piomelli, U., "Two-Layer Approximate Boundary Conditions for Large Eddy Simulations," *AIAA Journal*, Vol. 34, No. 6, 1996, pp. 1111–1119.

[40]del Alamo, J. C., Jimenez, J., Zandonade, P., and Moser, R. D., "Scaling the Energy Spectra of Turbulent Channels," *Journal of Fluid Mechanics*, Vol. 500, 2004, pp. 135–144.